Design and operation of transfer lines for plasma wakefield accelerators using numerical optimizers

R. Ramjiawan[*,†] S. Döbert, J. Farmer, E. Gschwendtner,
F. M. Velotti, L. Verra, and G. Zevi Della Porta

CERN, 1211 Geneva, Switzerland

V. Bencini[‡] and P. N. Burrows

John Adams Institute for Accelerator Science at University of Oxford, Oxford OX1 3RH, United Kingdom

The Advanced Wakefield (AWAKE) Experiment is a proof-of-principle experiment demonstrating the acceleration of electron beams via proton-driven plasma wakefield acceleration. AWAKE Run 2 aims to build on the results of Run 1 by achieving higher energies with an improved beam quality. As part of the upgrade to Run 2, the existing proton and electron beamlines will be adapted and a second plasma cell and new 150-MeV electron beamline will be added. The specification for this new 150-MeV beamline will be challenging as it will be required to inject electron bunches with micron-level beam size and stability into the second plasma cell while being subject to tight spatial constraints. In this paper, we describe the techniques used (e.g., numerical optimizers and genetic algorithms) to produce the design of this electron line. We present a comparison of the methods used in this paper with other optimization algorithms commonly used within accelerator physics. Operational techniques are also studied including steering and alignment methods utilizing numerical optimizers and beam measurement techniques employing neural networks. We compare the performance of algorithms for online optimization and beam-based alignment in terms of their efficiency and effectiveness.

I. INTRODUCTION

A. The use of optimizers in beamline design and operation

Numerical optimizers are powerful tools for beamline design and have been used at many particle accelerators; examples can be found in [1–5]. While there are many instances of using optimization algorithms to design optics or select settings of a pre-existing line, there are fewer that focus, as we do here, on optimizing the magnet positions as well as their strengths, see [6] for an example of this type of optimization.

The AWAKE experiment aims to produce a high-energy, low-emittance beam with a small energy spread as such a beam could have applications for an electron-proton

collider or for fixed target experiments. The design for the "witness" electron transfer line, used to inject bunches into the second plasma cell for acceleration, is therefore driven by these requirements. The specifications and constraints on the design, described in Sec. II A, are particularly challenging because of demanding beam size and stability requirements, as well as tight tolerances. Often, design optimization is done within beamline simulation tools like MAD-X [7]; however, we found that for our problem, the choice of optimization algorithms was too limited and there was insufficient control provided over the algorithms.

In this paper, we consider the various stages of the AWAKE electron transfer line design process and consider for each which numerical optimization algorithms and methods were most effective. In Sec. III A, we begin by designing a simplified transfer line comprising only dipoles and quadrupoles. We compare the performance of genetic algorithms for this task with the Nelder-Mead algorithm [8] and Powell's method [9]. We also study the interplay between the horizontal and vertical components of the objective function using multiobjective optimization.

In Sec. IV, we discuss the need for online optimization and possible algorithms for this. We study the suitability of the Bound Optimization BY Quadratic Approximation (BOBYQA) algorithm [10] for the beam-based alignment

---
[*]Also at John Adams Institute for Accelerator Science at University of Oxford, Oxford, United Kingdom.

[†]rebecca.louise.ramjiawan@cern.ch

[‡]Also at CERN, Geneva, Switzerland.

of the sextupoles and octupoles. For examples of the application of BOBYQA to online optimization problems see [11,12], and for alternative algorithms, see [13,14]. The performance of the BOBYQA algorithm is compared with that of the Robust Conjugate Direct Search (RCDS) algorithm [15] which was designed for optimization within a noisy environment.

We discuss the operational challenges expected for the witness electron line in Sec. V and highlight where machine learning or optimization techniques could be exploited. We overview a technique using physics-guided neural networks (PGNNs) to predict the electron beam trajectory, supplementing the limited available diagnostics with predictions from the optics model. Reconstructing beam parameters from limited diagnostics and the use of "virtual diagnostics" are common techniques in particle accelerators and examples of this can be found in [16–19]. We show results from testing PGNNs for beam trajectory prediction on the existing Run 1 beamline, compared with the performance of using only the optics model. Due to the challenging requirements for the electron beam alignment, described in Sec. II A, a technique like this to constantly and nondestructively measure the beam alignment will be crucial.

The AWAKE experiment is a proof-of-principle experiment and so, to fully study the plasma wakefield acceleration mechanism, it would be desirable to have the capability to scan the electron beam parameters to measure any dependencies. Therefore, a framework to frequently reoptimize the optics will be required. In Sec. VI, we consider the suitability of the Nelder-Mead algorithm for changing the optics of the witness transfer line and demonstrate the effectiveness of this algorithm for rematching the optics to incorporate two thin scattering foils.

B. AWAKE Run 1

The AWAKE Run 1 experiment at CERN demonstrated that electron beams could be accelerated to GeV-energies using plasma wakefield acceleration driven by self-modulated 400 GeV proton bunches [20,21]. The plasma was produced via the ionization of Rubidium in a 10-m long vapor cell with a high-power laser pulse, forming a 1-mm-radius plasma channel [22]. The wakefield driver consisted of a 400 GeV, 12-cm long proton beam from the CERN Super Proton Synchrotron (SPS) which was injected with a beam size of 200 μm into the plasma where it underwent self-modulation into a train of microbunches [23,24]. The microbunches had lengths approximately equal to half of the plasma wavelength and together resonantly drove large-amplitude plasma wakefields. The laser pulse used to ionize the plasma copropagated in the plasma cell with the proton driver beam and the self-modulation of the proton-bunch behind the laser pulse was seeded by the ionization front of the laser pulse. In this way, the proton bunch behind the laser pulse underwent the phase-reproducible seeded self-modulation (SSM) [25].

With a plasma electron density of 7×10^{14} cm^{-3}, the maximum accelerating gradient was of the order GV/m [26]. To probe the accelerating gradients of the wakefields, 18.84-MeV witness electron bunches were injected into the wakes [20]. The electron beamline comprised an S-band, rf photocathode gun producing electron bunches which were accelerated with a traveling-wave booster structure to 16–20 MeV. A transfer line [27] transported and focused these beams so that they could be injected on axis into the plasma cell with a beam size of 250 μm [28]. Electrons trapped in the focusing, accelerating phase of the wakefield were accelerated to 2.0(1) GeV [20], as measured with a magnetic spectrometer.

C. AWAKE Run 2

The goal of AWAKE Run 2 is to achieve acceleration to ~10 GeV while maintaining a smaller emittance and energy spread than Run 1 [29]. Toward this objective, Run 2 will be split into four intermediary stages [30]: (i) *2a*: demonstrate the seeding of the self-modulation of the full proton bunch with an electron beam to ensure modulation of the whole bunch is phase reproducible and stable [31], (ii) *2b*: introduce a density step in the plasma to stabilize the proton bunch self-modulation [32], (iii) *2c*: separate the proton bunch self-modulation and the electron bunch acceleration into separate plasma cells to isolate the defocusing fields of the unmodulated proton bunch from the electron bunch [33], and (iv) *2d*: demonstrate the scalability of the experiment to longer plasma cells and higher energies.

Run 2a studies the electron seeding of the proton bunch self-modulation and Run 2b will investigate the use of a density step to stabilize the self-modulation process; both of these features will then be incorporated into Run 2c.

In this paper, we discuss the studies toward the baseline design of the Run 2c transfer line needed to inject witness electron bunches into the second plasma cell to probe the accelerating gradients of the wakefields. The existing 18-MeV Run 1 electron line will be adapted to provide electron bunches to the first plasma cell to seed the self-modulation of the proton bunch. The parameters for this line will be determined as a result of the Run 2a studies.

A schematic of the proposed Run 2c beamline layout is shown in Fig. 1 showing the configuration of the proton and electron beamlines. Several changes will be needed to adapt the Run 1 experimental setup for Run 2c. To incorporate the additional seeding electron transfer line, the Run 1 plasma cell is to be moved 40 m downstream, requiring the reconfiguration of the proton beamline. To minimize the defocusing of the proton beam between the two plasma cells, the gap should be <1m [34], and ideally as short as possible, constraining the footprint of the witness transfer line. To achieve both a small energy spread and emittance conservation throughout acceleration, the injected electron beam parameters must be carefully chosen; this is discussed
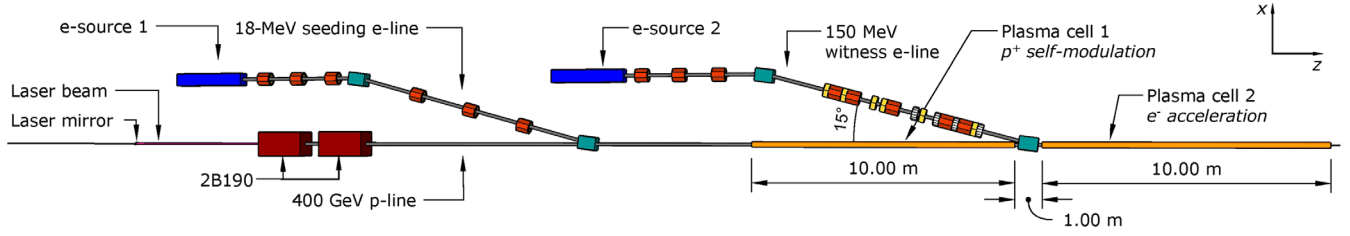
FIG. 1.   Schematic of the configuration of the two-electron beamlines, plasma cells, and a section of the proton transfer line. Dipoles are shown in cyan, the quadrupoles in red, the sextupoles in yellow, and the octupoles in white.

in Sec. II A [35]. The witness beam parameters for Run 2c compared with Run 1 are presented in Table I.

II. TRANSFER LINE DESIGN

A. Witness electron transfer line specifications

The specifications for beam parameters at the injection point derive from the need for the witness beam to be "matched" to the plasma to mitigate transverse betatron oscillations of the beam envelope propagating in the plasma which would cause emittance growth. For the electron beam to be matched to the plasma, the beam size should satisfy

$$\sigma^4 = \frac{2\varepsilon_0 m_e c^2 \gamma}{n_{pe} e^2} \epsilon^2, \tag{1}$$

where the Lorentz $\gamma = 293.5$, m_e is the mass of an electron, c is the speed of light, ε_0 is the vacuum permittivity, e is the electron charge, the normalized emittance $\epsilon = 2$ mm mrad, and the plasma density n_{pe} has baseline values: 2×10^{14} cm^{-3} or 7×10^{14} cm^{-3}. For beam energy of 150 MeV with the higher plasma density, this would correspond to a matched beam size of

$$\sigma^* = 5.75 \ \mu\text{m}. \tag{2}$$

Further specifications for the beam at the injection point are given in Table II.

The injected witness bunch should have a length of $\sim 60 \ \mu$m, a specification deriving from the need to be within the regime of optimal beam loading so that a small energy spread is conserved during acceleration [35,36]. To minimize emittance growth throughout acceleration, there

should be sufficient charge density in the witness bunch to be able to drive a full blowout of the electrons remaining in the plasma wakefield "bubble" [35]. The emittance growth during electron acceleration increases quickly with the transverse relative offset between the proton and electron beam. Simulations of the witness beam propagation in the plasma have shown that, for a nominal 2-mm mrad emittance beam to maintain an acceptable beam quality, the relative beam offset should not exceed 13 μm and the beam size should not exceed 1.5 times the nominal value [37].

The footprint of the witness beamline is constrained by the placement of the two plasma cells, the limited tunnel width, and the location of the seeding electron beamline. This constrains the width of the beamline to <3 m and the length to <25 m; a two-dipole dogleg design was selected to satisfy these restrictions. The dimensions of the dogleg are determined by the position and bending angle of the dipoles.

A 15° bending angle was selected as this was large enough that the beam pipe would not intersect with the plasma cell but not so high that the beamline exceeded the tunnel width. For a two-dipole achromatic dogleg, the first-order isochronous parameter, R_{56}, cannot be compensated, so that the transfer line would not be both achromatic and isochronous. To meet the bunch length specification of $\sigma_z = 60 \ \mu$m at the plasma injection point, it is proposed that the line have a shortening effect on the bunch, counteracted by injecting a correspondingly longer bunch into the transfer line. For the transfer line to have a shortening effect on the bunch, there must be a positive correlation between energy and longitudinal position,

TABLE I.   Beam parameters of the witness electron transfer lines for AWAKE Runs 1 and 2c [20,36].

Parameter	Unit	Run 1	Run 2c
Beam energy	MeV	18.84	150
Charge	pC	656	100
Bunch length	fs	4000	200
Energy spread	%	0.5	0.2
Normalized emittance	mm mrad	11–14	2

TABLE II.   Specification for the bunch parameters at the injection point of the AWAKE Run 2c witness transfer line.

Parameter	Specification
$\beta_{x,y}$	4.87 mm
$\alpha_{x,y}$	0.0
$D_{x,y}$	0 m
$\sigma_{x,y}$	5.75 μm
σ_z	60 μm
$\epsilon_{x,y}$	2 mm mrad

which based on simulations of the electron injector is expected to be feasible.

B. Transfer line simulations

The simulation code MAD-X [7] was used to model the beam transport, with the bunch tracking simulation using a MAD-X implementation of PTC (polymorphic tracking code) [38]. The nonlinear effects were challenging for this design, so six-dimensional particle tracking was essential for modeling the behavior of the line.

Simulations of the electron injector were used to produce an input bunch which was tracked through the transfer line to calculate the beam parameters at the injection point. The input bunch had 100,000 macroparticles and was designed such that the distributions in the x, y, p_x, and p_y planes were Gaussian distributions cut at 3σ, with standard deviations matching simulations of the beam from the electron injector. The E-z distribution was taken from the electron injector simulation and scaled to match the nominal Run 2 bunch length and energy spread, thus preserving the simulated correlation from the electron gun.

C. Numerical optimization for transfer line design

Optimization is the problem of finding a set of inputs for an "objective function" which corresponds to a maximum or minimum of that function. An optimization algorithm specifies the method used to iteratively choose inputs, evaluate the objective function, and compare solutions with the aim of moving toward the optimal solution. If multiple parameters need to be optimized, a single objective function can be formed as a weighted sum of the individual objectives ("scalarization") or they can form multiple objective functions (multiobjective optimization). For the design of the witness transfer line, both single- and multiobjective optimization were tested. Multiobjective optimization problems seek to optimize two or more objective functions simultaneously. If there is not a single solution that simultaneously optimizes all objectives, a set of optimal solutions called a "Pareto set" may be found.

The objective functions were adjusted at every step of the design process to take into account the current status of the design. For example, as the design progressed, higher order parameters became increasingly important and their weightings in the objective function were increased. The objective functions were formed as a weighted mean squared error (MSE),

$$\frac{1}{n}\sum_{t=1}^{n} w_i(y_i - y_{i,\text{target}})^2, \qquad (3)$$

where w_i are weights, and y_i and $y_{i,\text{target}}$ are the simulated and target parameters, respectively. Depending on the progress of the design, $y_{i,\dots,n}$ may include parameters such as the beam size, dispersion, or Twiss parameters. The input

variables and target parameters were each normalized by their respective maximum values.

Simulations of the electron propagation in plasma have shown that the beam distribution at the injection point is an important parameter for maintaining a high beam quality during acceleration. In order to optimize the beam distribution, the Kullback-Leibler (KL) divergence [39] was used to quantify the difference between the tracked bunch distribution and an ideal distribution. The K-L divergence is defined as

$$D_{KL}(p||q) = \sum_{i=1}^{n} p(x_i) \log\left(\frac{p(x_i)}{q(x_i)}\right), \qquad (4)$$

where $q(x)$ is the distribution under test and $p(x)$ is the true distribution. This was particularly useful for producing transfer line designs where the injected bunch needed to be Gaussian in six dimensions (x, p_x, y, p_y, z, p_z). Alternatively, if, rather than a Gaussian beam, a higher charge density is needed in the bunch core, then this corresponds to a high-kurtosis design, where the kurtosis is a measure of the tailedness of the distribution, defined as $\text{Kurt} = \mu_4/\sigma^4$, where μ_4 is the fourth central moment and σ is the standard deviation. In this case, the kurtosis was a helpful parameter to include in the objective function. For the AWAKE Run 2c experiment, the effect of the beam distribution on the quality of the acceleration is important to study and, so, being able to optimize the optics to achieve a given distribution or kurtosis would be helpful.

For the initial design stages, the simulations were performed with fewer macroparticles, sacrificing accuracy for speed. Once a coarse solution was found, fine-tuning was performed with a larger number of macroparticles. An essential parameter to include in the objective function was the fraction of the macroparticles lost throughout the transfer line due to aperture constraints. When optimizing magnet positions, it was also important to heavily penalize the overlap of magnets in the model.

D. Optimization problems

The choice of the optimization target and the way it is calculated make this a black-boxlike optimization problem. The code is not differentiable which constrains the choice of algorithms to derivative-free optimizers, random search algorithms, and genetic algorithms. A range of optimization algorithms was used throughout the design process for the Run 2c witness transfer line. When selecting an optimization algorithm, considerations may include whether there are constraints on the input variables or objective functions, the cost of each function evaluation, and whether the function is convex. A brief overview of the main optimization algorithms used for this design is given below.

(a) Genetic Algorithm A genetic algorithm (GA) is an optimization method based on a natural selection process akin to biological evolution. A population is a group of

individual solutions and at each step, the GA randomly selects individuals from the population and uses them as "parents" to produce the "children" for the next generation. GAs use three basic operators: selection, crossover (mating), and mutation; over successive generations, the population evolves toward an optimal solution [40,41].

Nondominated Sorting Genetic Algorithm II (NSGA-II) [41] is a multiobjective optimization algorithm using GAs, exploiting the concept of dominant and nondominant solutions to help quantify the fitness of solutions in a population.

(b) Powell's method A gradient-free, unconstrained optimization algorithm that minimizes a function by using sequential line searches along search vectors, often the axes of the input variables [9]. After each line search, the algorithm moves to the minimum found before progressing to the next vector.

(c) Nelder-Mead The Nelder-Mead algorithm is a search method to find the optimum value of an objective function in an n-dimensional space by using a simplex shape to explore the domain [8]. At each iteration, one vertex of the simplex moves toward a more optimal solution, where for each step, several possible adjustments may be tested before one is selected.

(d) BOBYQA The Bound Optimization BY Quadratic Approximation (BOBYQA) algorithm [10] uses a quadratic approximation to the objective function $F(x)$ at each iteration. It seeks to minimize $F(x)$ while respecting the bounds a_i and b_i,

$$a_i \leq x_i \leq b_i, \qquad i = 1, 2, \ldots, n. \tag{5}$$

BOBYQA is particularly useful for problems where evaluations of the objective function are time consuming, computationally intensive, or costly.

III. DESIGN OF THE RUN 2C WITNESS TRANSFER LINE

The full design of the witness transfer line was created over several intermediary stages, with the optimization algorithm and objective function adapted for each specific stage. To begin with, a transfer line design was produced from only dipoles and quadrupoles. The dipole position and bending angle were fixed by the desired geometry of the line and the quadrupole strengths and positions were the variables to be optimized. As the design for the transfer line progressed, nonlinear effects proved significant, requiring the addition of sextupoles and octupoles. These were added sequentially as required and the transfer line was iteratively reoptimized until a design was achieved which met the experimental specifications. The process used to evaluate the objective function and the full optimization process are presented in pseudocode in Algorithms 1 and 2, respectively, found in the Appendix.

A. Optimization of quadrupole positions and strengths

Typically for a transfer line with a very small focal point, the distances between the final focusing magnets and the focal point are minimized so as to reduce chromatic contributions to the beam size. Due to the proximity of the transfer line to the plasma cell (Fig. 1), to prevent the intersection of the final quadrupole with the plasma cell, the distance between the quadrupole and the focal point must be at least 1.9 m.

An initial transfer line design was constructed with the two dipoles, a quadrupole triplet before the dogleg, and five quadrupoles within the dogleg. The triplet was intended to focus the beam to a waist before the dogleg so that the dogleg can transport the waist to the injection point. To quantify the performance of the transfer line, a 6D beam distribution was tracked through the beamline to the injection point. The input variables for optimization were the positions and strengths of the eight quadrupoles. Within the dogleg, the symmetric pairs of quadrupoles have strengths of equal magnitude so there were 14 dimensions to the optimization problem.

Initially, the tracked beam distribution had only 5000 macroparticles which were increased at later stages. To produce a coarse initial design, only a reduced set of parameters was included in the objective function to prioritize the most challenging and important parameters for the overall design. The objective function, Eq. (6), included the horizontal and vertical beam sizes (σ_x, σ_y), dispersion (D_x, D_y) at the injection point, and the number of particles lost (N_{loss}). The number of particles lost was heavily weighted to penalize the algorithm if the beam envelope exceeded the apertures. Any overlap between magnets was penalized with a large weight to the whole objective function, M. A logarithmic transformation was used to aid convergence,

$$\begin{aligned} f_0(x) = M \log\{ & w_1(\sigma_x - \sigma_x^{\text{target}})^2 + w_2(\sigma_y - \sigma_y^{\text{target}})^2 \\ & + w_3(D_x - D_x^{\text{target}})^2 + w_4(D_y - D_y^{\text{target}})^2 \\ & + w_5 N_{\text{loss}} \}. \end{aligned} \tag{6}$$

As a first step, a GA was tested to try to find a global minimum. A population size of 200 with 300 offspring per generation was used. The mutation distribution index was set to 20 to encourage the exploration of the parameter space and to prevent the algorithm from getting trapped in local minima. The evolution of the mean objective function with successive generations of the GA is presented in Fig. 2 where the minimum objective function in the generation decreased over $\sim$60 generations before stabilizing. The solution corresponding to the minimum objective function evaluation had horizontal and vertical bunch sizes at injection of 17.6 and 30.9 μm, respectively. The bunch distributions at the injection point are presented in Fig. 3
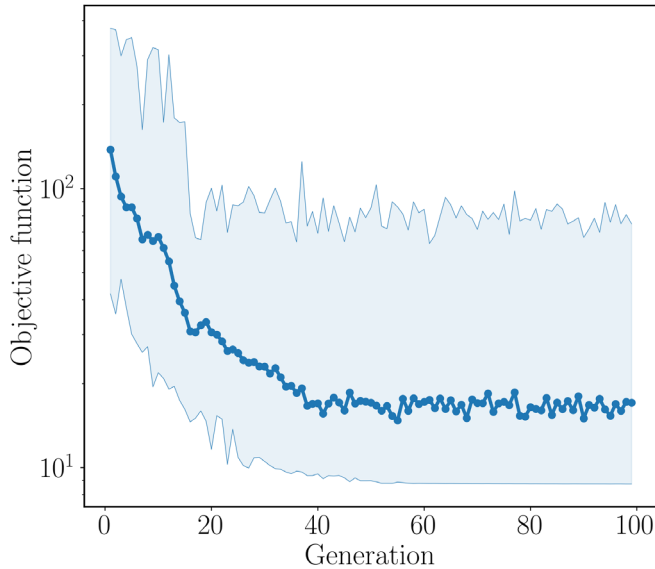
FIG. 2. Mean (data points) and range (shaded region) of the objective function evaluations from a population of solutions used by a genetic algorithm for the optimization of quadrupole strengths and positions.

with the macroparticles color-coded by their $\Delta E/pc$ values, highlighting the chromatic contributions to the beam size. In order to minimize the beam size, this effect was mitigated by the addition of sextupoles to the design.

Results from testing a GA for optimizing this transfer line design suggested that the horizontal and vertical beam

sizes could each be reduced but at the expense of the other plane. To investigate the limits for minimizing the beam sizes, the multiobjective optimization algorithm NSGA-II was used to optimize the horizontal and vertical parameters in Eq. (6) separately. Figure 4 shows the results from 250 generations with a population of 100, after which the final Pareto front was found to be in good agreement with the single-objective GA results. Figure 4 shows that even when minimizing the horizontal and vertical beam sizes independently, it is not possible to satisfy the experimental requirements. Separately, horizontal and vertical beam sizes of 16.0 and 20.8 μm were achieved, neither of which meet the target of 5.75 μm.

To compare the performance of GAs with other optimization algorithms, this optimization was performed also using the Nelder-Mead algorithm and Powell's method; the results are presented in Fig. 5. The performance of these algorithms is heavily dependent on the initial values, requiring the algorithms to be restarted 20 times with random initial conditions. The best solution found with the Nelder-Mead algorithm corresponded to $\sigma_x = 19.4$ μm and $\sigma_y = 48.9$ μm, and with Powell's method, $\sigma_x = 19.6$ μm and $\sigma_y = 42.4$ μm. It can be seen in Fig. 5(a) that GAs achieve the lowest value of the objective function. It should be noted that Fig. 5(b) shows the number of function evaluations for single applications of the Nelder-Mead and Powell's method algorithms, thus not taking into account the need to restart these algorithms multiple times. Considering the total evaluations from the 20 applications, the Nelder-Mead algorithm used 32000 total evaluations and Powell's method used 86000 iterations.
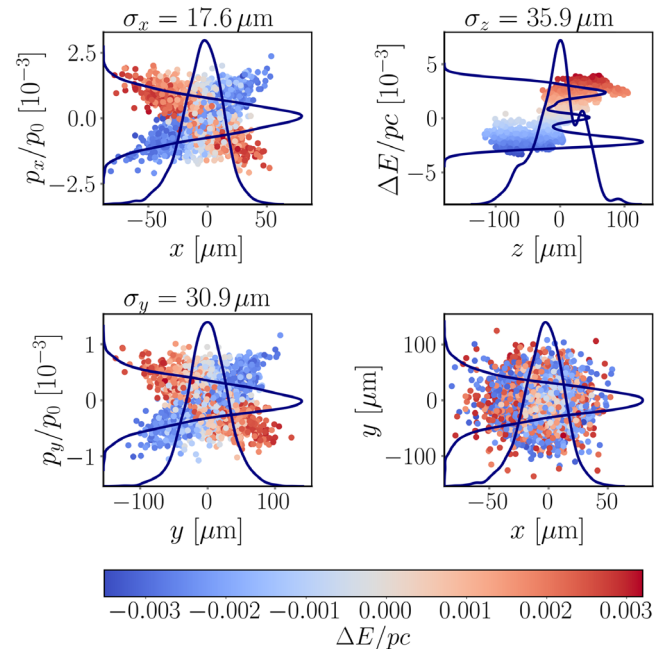

FIG. 3. 2D projections of the distribution of a bunch tracked through the transfer line to the plasma injection point. The color of the data points denotes the $\Delta E/pc$ value.
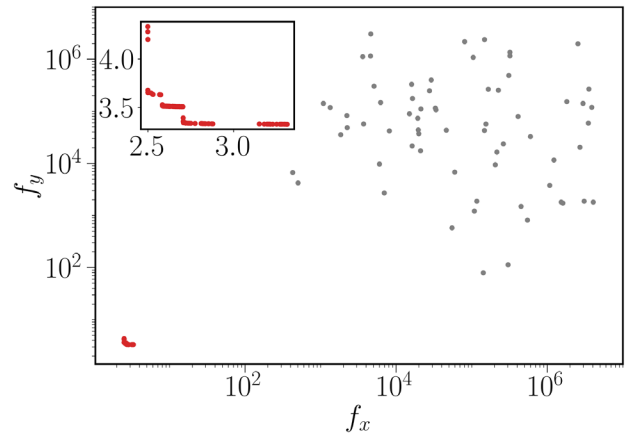

FIG. 4. Points on the Pareto front at the final evaluation (red) and the population from the first evaluation (gray) of the multiobjective optimization of quadrupole strengths and positions; the axes are the two objective functions constructed from the horizontal and vertical components of Eq. (7). The inset shows an expanded view of the final Pareto front. Only viable solutions with no magnet overlap are included.
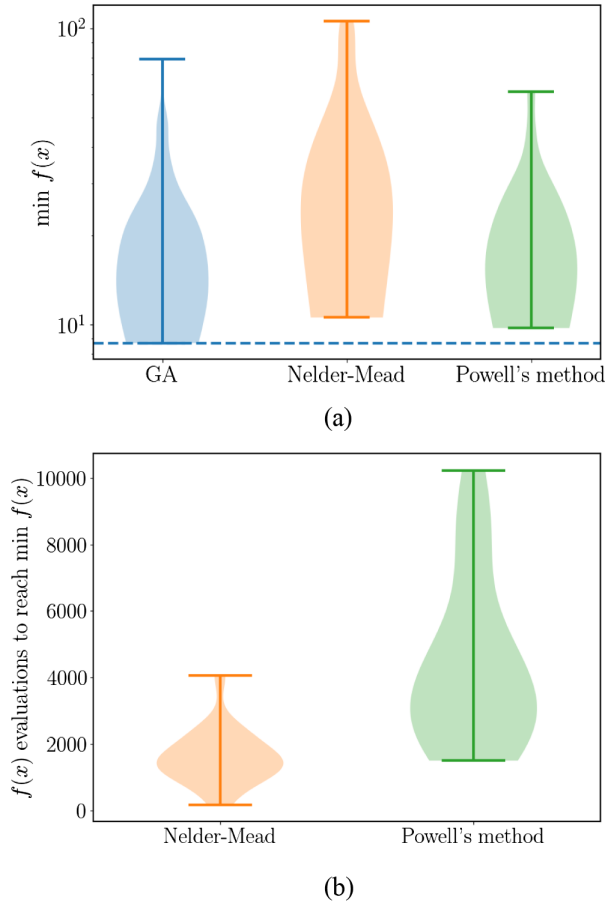
(a)

(b)

FIG. 5. (a) The minimum objective function $[f(x)]$ values from the optimization of quadrupole strengths and positions using GAs, the Nelder-Mead algorithm and Powell's method. The Nelder-Mead algorithm and Powell's method were started 20 times with random starting values. The minimum and maximum values for each are indicated. (b) The number of function evaluations to reach the minimum $f(x)$ for each of the 20 optimization attempts.

B. Addition and optimization of sextupoles and octupoles

To combat the chromatic contributions to the beam size at the injection point, sextupoles were added, initially chosen to be at regions of high D_x/x and D_y/y and at phase advances to have maximum impact at the injection point. The sextupole positions were then included, along with the strengths of the sextupoles, in the list of inputs for the optimization algorithm. Powell's method proved to perform well for this stage, as it coped well with the high dimensionality and was explorative of the parameter space. Once an initial optimization of the layout of the transfer line with sextupoles had been performed, finer adjustments were made, for which the weights in the objective function were adjusted and higher-order parameters like $\alpha_{x,y}$, $D'_{x,y}$ and the K-L divergence were included or given a higher weighting. This objective function could be written as
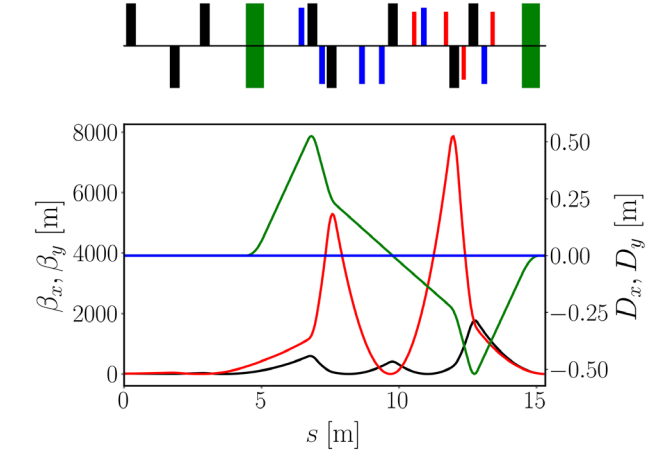

FIG. 6. MAD-X simulation of the transfer line design after the optimization of the sextupole and octupole positions and strengths. Twiss parameters β_x (black), β_y (red), and dispersion D_x (green) and D_y (blue) are shown below, with a synoptic overview of the transfer line above, with dipoles (green), quadrupoles (black), sextupoles (blue), and octupoles (red).

$$
\begin{aligned}
f_1(x) = M \log\{ & w_1(\sigma_x - \sigma_x^{\text{target}})^2 + w_2(\sigma_y - \sigma_y^{\text{target}})^2 \\
& + w_3(D_x - D_x^{\text{target}})^2 + w_4(D_y - D_y^{\text{target}})^2 \\
& + w_5(\alpha_x - \alpha_x^{\text{target}})^2 + w_6(\alpha_y - \alpha_y^{\text{target}})^2 \\
& + w_5 N_{\text{loss}} + w_6 \text{KL}_{\text{div}} \},
\end{aligned} \tag{7}
$$

where $\alpha_{x,y}$ are Twiss parameters and KL_{div}. is the K-L divergence.

Even after a solution was found for which the sextupoles would mitigate the chromatic effects, there were remaining detuning with amplitude effects contributing to the beam size. Without the addition of octupoles to correct for these effects, it seemed impossible to reduce the beam size below 8 μm either horizontally or vertically. Octupoles were added incrementally and their positions and strengths were optimized using the same process as for the sextupoles. Detuning with amplitude effects could not be corrected locally throughout the entire line, so the focus was on reducing these effects at the injection point. The optics for the resulting transfer line is presented in Fig. 6 showing the final placements of the six sextupoles and four octupoles. The beam parameters at the injection point are given in

TABLE III. Beam size and linear optics parameters at the injection point for the transfer line shown in Fig. 6.

Parameter	x plane		y plane
$\sigma_{x,y}$ (μm)	6.0		6.1
σ_z (μm)		59.9	
$\beta_{x,y}$ (mm)	4.8		5.4
$\alpha_{x,y}$	0.0		0.0
$D_{x,y}$ (m)	0.0		0.0

Table III, showing that this transfer line design meets experimental requirements for the beam size. For the transfer line to meet the nominal bunch length, $\sigma_z = 60\ \mu$m, the input bunch length should be 40% longer.

IV. BEAM STEERING AND ALIGNMENT

To understand the impact of sources of error or misalignment on the beam parameters, studies of the errors individually were performed and used to specify upper bounds on the error tolerances. For example, tracking simulations as a function of the magnitude of the quadrupole misalignments are presented in Fig. 7 showing that, after beam-based alignment and steering have been performed, a beam-quadrupole alignment of better than 10 μm should be achieved. Similar studies for other error sources were used to determine suitable values to be used for error studies of the transfer line, these values are given in Table IV. The magnet misalignments specified in the table are before any beam-based alignment has been performed.

To achieve the required levels of magnet beam alignment, the magnets would need to be on movers with a step size of approximately 1 μm and with a range of 100 s of microns. Multiple steering and alignment methods will be required. From simulations of the transfer line in the presence of the errors in Table IV, a procedure for beam-based alignment was developed. The locations of the beam position monitors (BPMs), beam screens (BTVs), and correctors for this process are indicated in Fig. 8. First, it is proposed to use a quad shunting technique, varying the quad strength (between 80% and 100%) and measuring the deflection of the beam at a downstream BPM. This deflection could be used to estimate the beam-quadrupole offset to be corrected with the magnet mover. Dispersion free steering (DFS) would then be used to minimize the parasitic dispersion by using the correctors to steer the beam through the center of quadrupoles. With DFS, the

beam offset is measured at all BPMs at different beam energies, the beam is then steered to both minimize the offset of the beam in the BPMs and to minimize the difference in trajectory for different beam energies. DFS is first performed with higher order magnets switched off. The deflections of the beam from sextupole or octupole offsets are likely to be difficult to resolve with the BPMs, although they will affect the beam size. Therefore, it is suggested to use the measured beam size at the injection point BTV to quantify their alignment. We proposed to use an optimization algorithm to align the sextupoles and octupoles offsets by minimizing the beam size at the injection-point BTV.

The proposal for a procedure for beam steering and alignment is given below and is estimated to be feasible in under an hour, (1) quadrupole shunt—two iterations, gain 0.7, (2) quadrupole shunt—one iteration, gain 1, (3) DFS—higher order magnets off—three iterations, gain 0.7, and (4) align sextupoles and octupoles using an optimization algorithm to vary magnet mover settings 100–400 iterations.

Multiple iterations of the quadrupole-shunting and DFS methods are performed with gains set lower than unity. This is desirable to prevent the alignment process from becoming unstable and also because the nonlinearity of the system is sampled better with smaller steps. A lower gain is also helpful to reduce the impact of the finite BPM and BTV resolutions.

For the beam-based alignment of the sextupoles and octupoles, the BOBYQA algorithm was employed because, as previously mentioned, it is a useful algorithm when function evaluations are costly. Specifically, the Py-BOBYQA [42] Python implementation of BOBYQA was used. The Py-BOBYQA implementation has a flag, `objfun_has_noise`, which should be set when the objective function has stochastic noise in order to increase the number of interpolation points used. Here, the lifetime of the magnet movers restrict the number of times their settings can be changed.
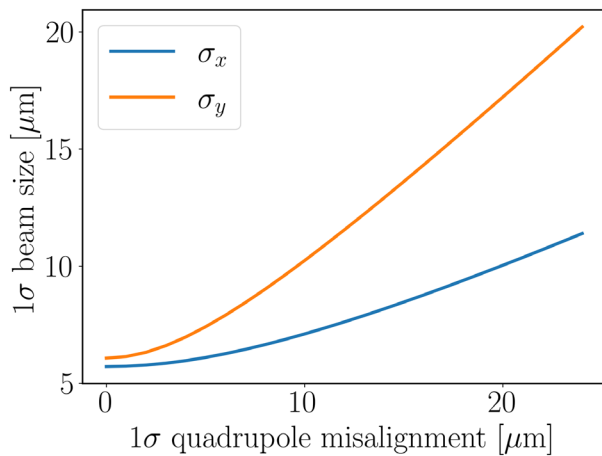

FIG. 7.   Horizontal and vertical beam sizes averaged over 50 seeds with quadrupole misalignments sampled randomly from a Gaussian distribution with standard deviation given by the x axis.

TABLE IV.   The rms values for the distributions of errors and resolutions used for simulations of the Run 2c witness transfer line.

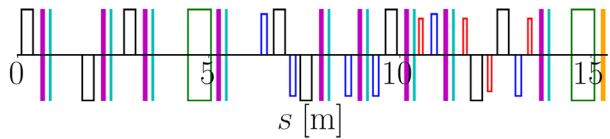| Parameter	Error	Unit
Magnet mover position	1	μm
Corrector kick	1	μrad
BPM resolution	10	μm
BTV beam size resolution	1	μm
BTV position resolution	10	μm
Momentum jitter	1000	ppm
Input position jitter	10	μm
Dipole misalignments	50	μm
Magnet field error	10	ppm
Quadrupole misalignments	100	μm
Sextupole misalignments	100	μm
Octupole misalignments	100	μm

FIG. 8.   Schematic showing the locations of BPMs (cyan), a BTV (yellow), and correctors (purple). Magnet positions are shown as outlines. The beam goes from left to right.

It may also be desirable to minimize the magnitude of the steps taken by the magnet movers so that large changes are avoided when possible.

We have compared the performance of Py-BOBYQA, with `objfun_has_noise` both `True` and `False`, with the robust conjugate direct search algorithm (RCDS) [15]. The RCDS algorithm was developed specifically for online optimization, for which the objective function may be noisy. The RCDS method is a combination of a conjugate

direct search (like Powell's method) and a 1D line optimizer to make it more robust against noise. The comparison between the methods is shown in Fig. 9. The Py-BOBYQA algorithm (`objfun_has_noise = False`) reaches a minimum value quicker than the other two methods, at the expense of a poorer minimum value. The median performance of Py-BOBYQA (`objfun_has_noise = True`) and RCDS is comparable in terms of both the minimum objective function evaluation and the number for iterations taken to reach it. If the BOBYQA algorithm was chosen, the setting of the flag `objfun_has_noise` would depend on whether speed or accuracy were more desirable.

After the setting-up procedure is performed, an efficient way to maintain the optimal conditions is to apply shot-to-shot feedback loops on trajectory using the available correctors. The change should be small enough not to significantly perturb the beam size. The same could also be
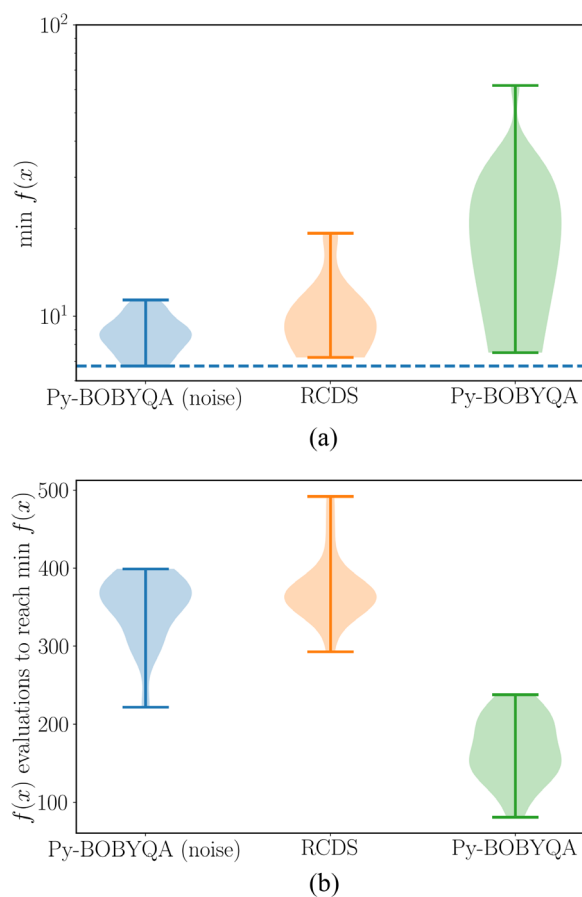

(a)

(b)

FIG. 9.   (a) The minimum objective function [$f(x)$] values from the minimization of the injection-point beam size by optimizing sextupole and octupole transverse offsets using (left) Py-BOBYQA (`objfun_has_noise = True`), (center) RCDS, and (right) Py-BOBYQA (`objfun_has_noise=False`). (b) The number of function evaluations to reach the minimum $f(x)$. The algorithms were tested on 20 error seeds; the minimum and maximum values for each are indicated.
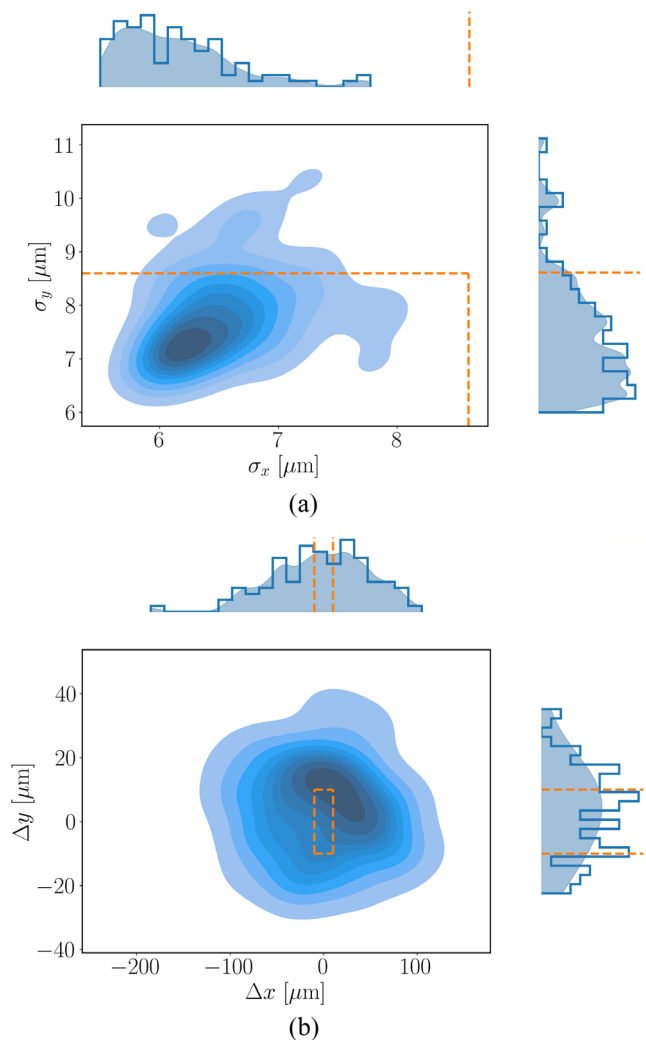

(a)

(b)

FIG. 10.   Distributions of (a) beam sizes and (b) relative proton-electron transverse bunch offsets at the injection-point for 100 seeds with errors as defined in Table IV after beam-based alignment. The orange lines denote the experimental specifications.

applied to the beam size, but the main problem there is measuring with a nondestructive technique.

Simulations of these alignment techniques were performed with the errors and resolutions specified in Table IV. As the relative proton-electron offset is of interest, also modeled was the proton beam jitter, with 81.7 μm and 10.5 μm rms jitter in the horizontal and vertical planes, respectively. The proton beam jitter was determined from measurements of the Run 1 jitter scaled for the Run 2 configuration. About 100 seeds were simulated and after the full process of beam-based alignment, 85% of seeds satisfied the experimental beam size requirements [Fig. 10(a)] and 6% satisfied the relative offset tolerances [Fig. 10(b)]. It should be noted that the proton beam jitter was the dominant source of the offset between the beams, with the electron beam jitter and static misalignment contributing only a few microns.

V. BEAM TRAJECTORY RECONSTRUCTION USING NEURAL NETWORKS

As described in [37], the alignment of the AWAKE driver and witness beams is critical. This will require a method to measure the proton and electron trajectories through the plasma cell constantly during operation. During operation, the injection-point BTV cannot be used and, instead, the beam trajectory through the plasma cell should be reconstructed from the diagnostics which are available.

In this section, we describe how physics-guided neural networks (PGNNs [43]) could be used to estimate the beam alignment of the witness and seeding electron beams when direct measurements are not possible. Although the full design for the seeding line has not been completed, it is expected to be similar to the Run 2a electron line and consequently face similar issues. Here we propose a dedicated beam measurement technique for the relative proton-electron alignment for Run 2c. In order to demonstrate the effectiveness of this method, we describe tests of using this method on the Run 2a experiment.

Within the AWAKE Run 2a common line (Fig. 11), in which the electron and proton beams copropagate, the proton beam dominates the BPM signals so that electron measurements are not possible while there are protons. Additionally, the signals from the BPMs closest to the plasma cell are corrupted in the presence of plasma and cannot be used for either protons or electrons. Without these measurements, the beam trajectory through the common line needs to be reconstructed based on measurements from upstream BPMs. There is ongoing work to study whether it would be possible to use a BPM exploiting Cherenkov diffraction radiation to simultaneously measure the electron and proton beam positions [44]. If such a BPM were to become available operationally in the AWAKE electron line, this could be incorporated into the PGNN reconstruction method.
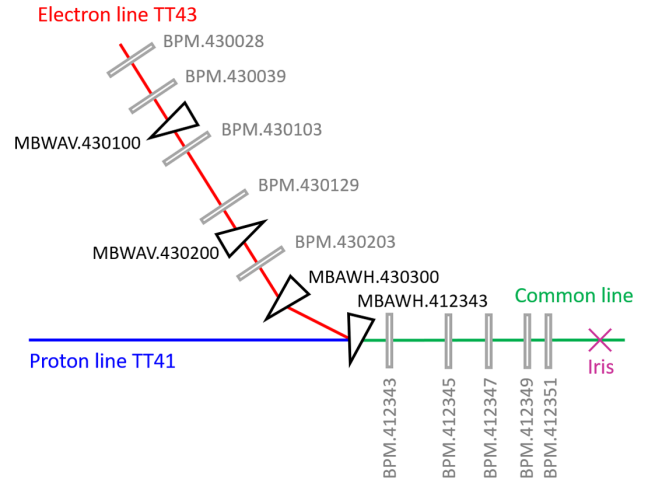

FIG. 11. Schematic of the proton beamline (blue), electron beamline (red), and common line (green). The relevant BPMs are shown as rectangles and the electron line dipoles as triangles; quadrupoles are not shown in this diagram. The beams propagate from left to right. The iris marker highlights the start of the plasma.

The Run 2a ~18-MeV electron beamline (TT43) is used to inject bunches on axis into the plasma cell. The electron beamline has five BPMs before the common line and five BPMs within the common line (Fig. 11). The beam trajectory, as characterized by measurements from the first five BPMs, can be propagated into the common line using the optics model and these studies are summarized in [45]. This study concluded that with this method, the beam position could be predicted at the final BPM, BPM.412351, with rms errors of ~370 μm horizontally and ~150 μm vertically. Here, we describe a method to improve these predictions with the addition of PGNNs.

A. Beam trajectory predictions

PGNNs use predictions from a physics model of the system alongside measured data as the inputs to the NN. In cases where the measured data are inaccurate or noisy, the physics model may give better prediction, whereas, if the model has significant shortcomings in representing the system, the measured data would be more trustworthy.

The beam trajectory through the common line can be predicted for every pulse by propagating the electron trajectory using the transfer line model with the following method. First, with the plasma off and no proton beam, the mean beam trajectory was measured at all ten BPMs in the electron line. The mean trajectory was subtracted from the measurements so as to keep the pulse-to-pulse variation only. Second, the momentum offset, δ_p, was calculated for every pulse, using the method described in [46], by exploiting that the BPMs, BPM.30103 (103), and BPM.430129 (129), have a phase advance of almost π between them so that,
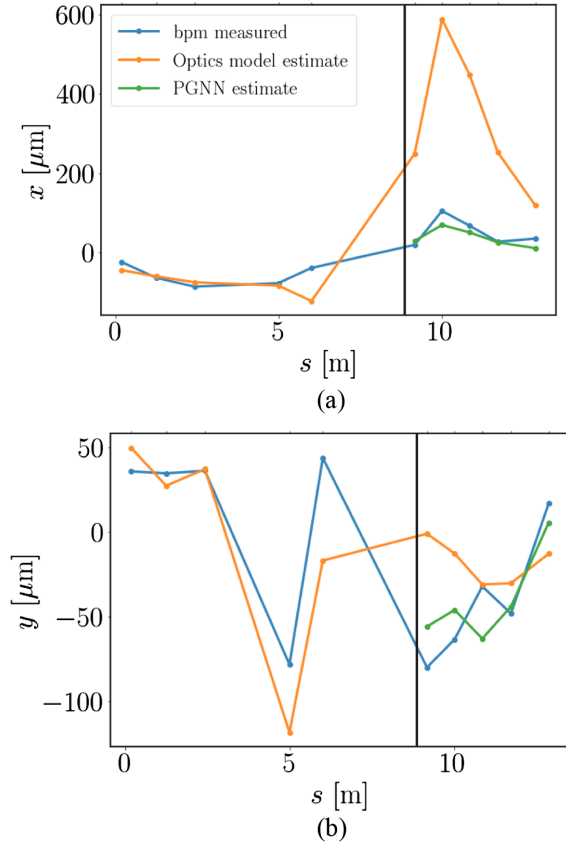
FIG. 12. A comparison of the optics model beam trajectory prediction (orange) and the PGNN prediction (green) with the measured high-charge BPM data (blue), shown for the horizontal (a) and vertical (b) planes. The start of the common line is denoted by a vertical black line.

$$\delta_p \simeq \frac{\sqrt{\beta_{103}}\,y_{129} + \sqrt{\beta_{129}}\,y_{103}}{\sqrt{\beta_{103}}\,D_{129} + \sqrt{\beta_{129}}\,D_{103}}. \qquad (8)$$

From δ_p, the dispersion contribution was calculated and subtracted from the beam trajectory leaving the betatron contribution. The optics model was used to propagate the betatron contribution into the common line and, finally, the dispersion component and mean trajectories were added back to get beam position estimates. The predicted beam trajectories for a representative pulse are shown in Fig. 12. The discrepancy between the horizontal trajectory measurements and predictions, seen in Fig. 12, was due to a difference between the optics model and the beamline, where in [45], this is hypothesized to be an offset of quadrupole 430311.

A PGNN was tested to predict the residual errors from the optics model propagation of the beam trajectory. The PGNN had 30 features consisting of the first 5 BPM measurements, both horizontally and vertically, and the corresponding beam trajectory predictions for all 10 BPMs. The input values

$$[x_1^{\mathrm{meas}}, ..., x_5^{\mathrm{meas}}, x_1^{\mathrm{pred}}, ..., x_{10}^{\mathrm{pred}},$$
$$y_1^{\mathrm{meas}}, ..., y_5^{\mathrm{meas}}, y_1^{\mathrm{pred}}, ..., y_{10}^{\mathrm{pred}}]. \qquad (9)$$

were normalized to lie in the range of 0–1. The NN output comprised the errors on the optics model predictions compared with the BPM measurements for the final five BPMs,

$$[x_6^{\mathrm{meas}} - x_6^{\mathrm{pred}}, ..., x_{10}^{\mathrm{meas}} - x_{10}^{\mathrm{pred}},$$
$$y_6^{\mathrm{meas}} - y_6^{\mathrm{pred}}, ..., y_{10}^{\mathrm{meas}} - y_{10}^{\mathrm{pred}}]. \qquad (10)$$

As the PGNN output is compared with BPM measurements to calculate the PGNN output error, the resolution of the BPMs sets a limit to the PGNN performance that can be measured. To propagate the predictions from the BPMs to the iris, the beam angle was calculated from the ballistic trajectory through the final two BPMs. This propagation should take into account the effect on the beam trajectory from the Earth's magnetic field.

The PGNN had six hidden layers with the number of nodes per layer stepping from 30 to 60 and back to 30 in steps of 10. The hidden layers had tanh activation functions. During training, the learning rates were decreased stepwise throughout training and this process was optimized empirically. The data were split 80%/20% into training and test data sets. Of the training data, 10% were used as a validation set to optimize the hyperparameters and highlight any overfitting of the model. A batch size of 64 was used for training and of order 1000 epochs. An MSE loss was used to quantify the PGNN performance.

B. Results

PGNNs were tested on data at three different charges, 300, 650, and 750 pC, as measured with a Faraday cup. The BPM resolution scales with the BPM signal-to-noise ratio and, consequently, with the beam charge so that these data could be used to study the variation in PGNN performance with BPM resolution. Three separate NNs were trained for the three charges. The 750 pC data set had ∼4000 events with 80% used for training and validation. The training was performed over 1500 epochs as the MSE loss typically converged in 1000–1500 epochs. The predictions of the PGNN compared with the measured data and optics model prediction are given in Fig. 12 for a single test event. The PGNN performances at BPM 51 are shown in Fig. 13 for the three charges, where the degradation in measured PGNN performance with decreasing charge can be seen. The AWAKE BPMs are expected to have resolutions of up to 20 μm which agree well with the high-charge results.

For the low charge data, the BPM signal level was approximately a tenth of that for the high charge data. With this lower resolution, neither the optics model prediction nor the PGNN prediction is measured to perform much better than the level of the beam jitter. This is likely a result
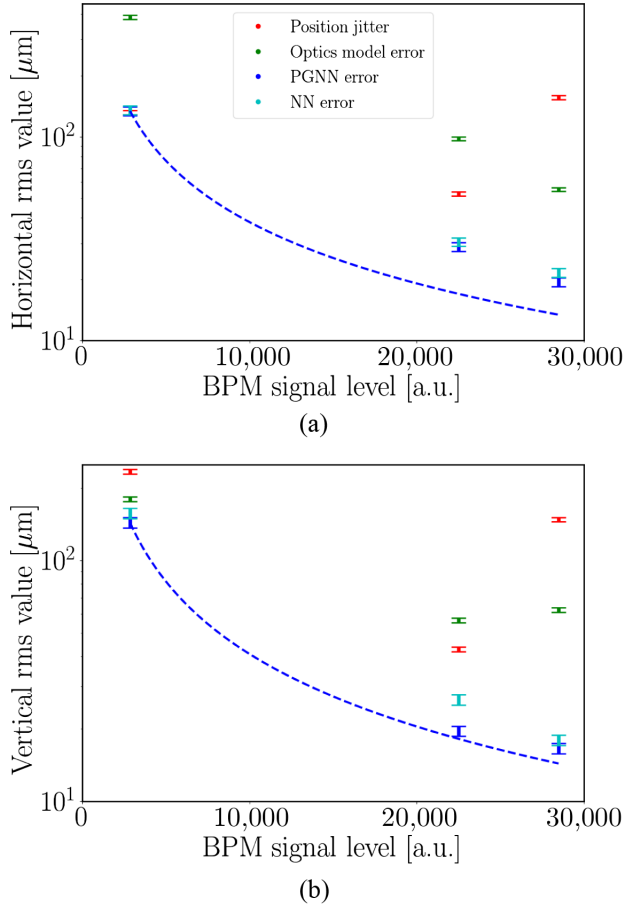
(a)

(b)

FIG. 13. The data points show the horizontal and vertical rms values for beam jitter and position predictions at BPM 51; the error bars give 95% confidence interval. The resolution scaling from the low charge is given as a dashed line under the assumption that the low-charge results were resolution limited. The NN error denotes the error from a neural network without including predictions from the beamline model.

of the BPM resolution being of the same order as the measured beam jitter, meaning that the jitter measurements are resolution limited. In this case, better results may be achieved by assuming always the mean beam trajectory

rather than trying to predict the trajectory pulse-to-pulse. For the horizontal predictions at BPM 51 [Fig. 13(a)], the optics model estimates for the end of the line give poor results, and thus the inclusion of these as inputs to the NN yields no additional improvement. In the vertical plane, the improvement from the inclusion of the optics model to the NN is 10–20%.

The resolution is expected to scale linearly with the BPM signal-to-noise ratio, where the sums of the BPM signals for the three charges were 2850 arb. units (300 pC), 22500 arb. units (650 pC), and 28500 arb. units (750 pC). The best PGNN performances, as measured at BPM 51, are presented in Fig. 13 along with the estimated resolution scaling calculated by assuming the performance of the low-charge case was resolution limited. There is good agreement vertically but horizontally the higher charge predictions underperform compared to the resolution scaling. The BPMs with the largest horizontal jitters also demonstrate the poorest horizontal predictions, requiring further study.

The results from propagating the beam trajectory to the iris are presented in Table V. There is a clear improvement in the position and angle predictions at medium and high charge with the PGNN. The resolution of the position measurement extrapolated to the iris can be calculated from the geometry of the system. This can then be compared with the measured PGNN performance. For example, if the final two BPMs have a resolution of 20 μm at high charge, this would correspond to a 48-μm resolution at the iris. The PGNN error propagated to the iris is in good agreement with this. If we assume that the low-charge results are resolution limited, then the final two BPMs have a resolution ~140 μm, which would correspond to a 340-μm resolution at the iris.

It has been shown that PGNNs can be used to reconstruct the beam trajectory through the Run 2a AWAKE common line. This method could be adapted for use with the Run 2c seeding electron line and even developed into an application to give real-time predictions of the relative alignment between the proton and electron beams. Ideally, the Run 2c seeding electron line would also have BPMs in the dogleg

TABLE V. Angle jitter and position jitter propagated to the iris, both calculated using measurements at the last two BPMs. Comparison with the rms errors from the optics model predictions and PGNN model predictions.

	Horizontal			Vertical		
Charge	Low	Medium	High	Low	Medium	High
Angle jitter (μrad)	200	118	119	181	91	113
Angle optics error (rms) (μrad)	170	92	61	179	25	46
Angle PGNN error (rms) (μrad)	164	24	22	178	24	19
Iris jitter (μm)	604	161	488	495	182	194
Iris optics error (rms) (μm)	527	133	161	508	86	95
Iris PGNN error (rms) (μm)	446	69	58	496	66	53

at π-phase-advance so that the momentum offset could again be easily measured.

VI. SCATTERING FOILS

The AWAKE experiment will require two thin foils to be placed in the beamline just upstream of the focal point [47]. The first will be a vacuum window for the plasma cell and the second will be a dump for the laser used to ionize the second plasma cell. Due to the thickness and radiation length of the material traversed, and the energy of the beam, the main contributor to the change of emittance and optics is multiple Coulomb scattering. This translates into a net angular deflection from the original particle direction which can be modeled as Gaussian. The angular dispersion, θ_0 is given by [48]

$$\theta_0 = \frac{13.6}{\beta c p} z \sqrt{\frac{t_0}{X_0}} \left[1 + 0.038 \ln \frac{t_0}{X_0} \right], \qquad (11)$$

where c is the speed of light, $\beta = \frac{v}{c}$, p is the momentum in MeV/c, X_0 is the material's radiation length, and t_0 is the material thickness. The laser beam dump and vacuum window were modeled as two aluminum foils, with $X_0 = 8.9$ cm and 1 mm separation both between the two foils and between the final foil and the injection point.

The scattering of the beam within the foil causes the beam emittance to increase [49], with the emittance increase depending on the beta function at the foil. The beta function after the foil is reduced, thus requiring the optics to be reoptimized to return the beam focal point to the injection point.

The Nelder-Mead algorithm was tested for rematching the optics while keeping the magnet locations fixed. The Nelder-Mead algorithm proved useful for making small adjustments to the transfer line optics, typically finding a solution within a few hundred iterations. This framework could be used, for example, to adapt the optics to produce a larger beam size, alter the beam distribution, or shift the beam waist. It is foreseen that the AWAKE Run 2c experiment will scan the witness bunch parameters such as the beam size and waist position, so this capability is essential. The Nelder-Mead algorithm was selected as it is easy to use and understand. This is important because it will be used frequently during operation and possibly by those with limited experience in numerical optimization.

To ensure the emittance blowup in the x and y planes were equal, the term $|\sigma_x - \sigma_y|$ was incorporated into the objective function. The emittance after the scattering foil was left as a free parameter during optimization. The injection-point beam parameters for the rematched transfer line, including the scattering foils, are presented in Table VI. The injection-point beam sizes are 17.2 and

TABLE VI. Beam parameters at the injection point for a transfer line with two 100 μm aluminum foils.

Parameter	x plane	y plane
$\sigma_{x,y}$ (μm)	17.2	17.6
$\alpha_{x,y}$	0.0	0.0
$D_{x,y}$ (m)	0.0	0.0
$\epsilon_{x,y}$ (mm mrad)	17.0	16.9

17.6 μm horizontally and vertically, respectively, which are within approximately 5% of the matched beam sizes. The effect of this 5% beam size deviation on the emittance growth during acceleration would depend on the bunch charge and would be only a few percent.

VII. OUTLOOK

Genetic algorithms and numerical optimizers for beamline design are particularly useful for cases where considering only linear optics is not sufficient and accounting for all aberrations is nontrivial. Supervision is clearly still needed and any additional information, including constraints, is invaluable. Establishing constraints, often with a physical basis, can help converge toward more elegant solutions that are more robust with respect to errors.

Potential developments of this technique could be the employment of hierarchical structures in multilayer optimizers to further automate the design of transfer lines. This could include design optimization where the quantities and types of magnets are also determined by an optimizer. The ultimate goal would be a fully automatic design process, for which a complete beamline design is produced based on the desired start and end points, required beam parameters, and physical constraints.

The use of PGNNs for trajectory predictions is a very general concept for accelerators. As optics knowledge is frequently available, this could represent a way to circumvent invasive or expensive beam diagnostics. A natural way to extend this further would be to exploit raw BPM waveforms to try to estimate the beam size.

VIII. CONCLUSION

In this paper, we have described how numerical optimization and neural networks were used during the design of the AWAKE Run 2c electron transfer lines. The baseline design of a 150-MeV electron transfer line to inject witness bunches into the second plasma cell was presented. The spatial constraints and experimental requirements for micron-level beam size and stability were challenging and various optimization techniques were used during the design process.

GAs were exploited to produce an initial dogleg design comprising only dipoles and quadrupoles. Within 250 generations with a population of 100, a design with an injection-point beam size of 17.6 μm horizontally and 30.9 μm vertically was achieved. This did not meet the experimental specification of a 5.75-μm beam size and multiobjective optimization with the NSGA-II algorithm was used to analyze the interplay between minimizing the beam size horizontally and vertically. These results showed that the beam size requirements could not be met even when only considering a single plane. The performance using a GA was contrasted with the Nelder-Mead algorithm and Powell's method, each restarted 20 times with random starting values. The GA was shown to reach a smaller value of the objective function, with fewer function evaluations.

The strong focusing that was needed to produce small beam sizes led to the rise of significant nonlinearities, such as betatron chromatic effects and detuning with amplitude. Sextupoles and octupoles were added to mitigate these effects and their positions and strengths were optimized with Powell's method.

The effects of errors and misalignments on the beam size and stability were studied and a correction process was developed and simulated. These studies suggest that after beam-based alignment, 85% of the pulses should satisfy the experimental beam size specification. For the relative proton-electron beam misalignment, only 6% of pulses were within the tolerances, but this was dominated by the proton beam jitter. The optimization algorithm BOBYQA was studied for the beam-based alignment of the sextupoles and octupoles using beam size measurements from a BTV at the injection point. While this was successful in simulation, further studies into the feasibility of this method are required, in particular, accounting for the mover limitations and lifetime. The Py-BOBYQA implementation of the BOBYQA algorithm was compared with the RCDS algorithm in terms of the minimum objective function value and the number of function evaluations required. The median performance of the two algorithms was shown to be similar.

An optimization framework based on the Nelder-Mead algorithm was created which could facilitate the reoptimization of the transfer line optics if minor adjustments are needed. This was used to rematch the transfer line to include two thin scattering foils upstream of the focal point. These foils increased the emittance so that the matched beam size was 16.7 μm. The Nelder-Mead algorithm was selected due to its speed and ease of use.

Studies were also presented toward developing a method for reconstructing the electron beam trajectory through regions with no available direct position measurements. As the alignment tolerances for Run 2c are very challenging, such a method for continuously measuring the electron beam trajectory will be essential. A method suitable for Run 2c was tested on the Run 2a beamline and the addition of PGNNs was shown to offer significant improvements compared with using only the optics model. The results at high charge were consistent with the expected resolution limit of the BPMs, with PGNN rms errors at the final BPM of <20 μm. The performance of the vertical predictions at different charges scaled well with the expected resolution, however, the horizontal results deviated, thus requiring further study.

ACKNOWLEDGMENTS

APPENDIX: OPTIMIZATION PROCESS PSEUDOCODE

Algorithm 1: Calculation of the objective function used to optimize magnet positions (Pos) and strengths (Str).

```
/* Inputs are the magnets' positions and
strengths (x), which magnets to optimize
(magnetList), which parameters to include in
the objective function (objParams), and the
number of macro-particles to track
(nParticles)                              /*
```
1 **Function** Objective (*x*, *magnetList*, *objParams*, *nParticles*):
2   M ← 1; i ← 1;
3   **for** *magnets in magnetList* **do**
     set: magnetPos, magnetStrStr ← x[i]
4   i ← i + 1;
5   **end**
6   M ← overlap penalty;
7   if *tracking code error* **then**
8   f(x) ← penalty f(x);
9   f(x) ← f(x) × M;
     reset: tracking code
10   **return** f(x)
11   **end**
   track: nParticles
12   Calculate parameters at injection-point;
13   nLoss ← number of macro-particles lost;
14   **if** *nLoss > 0.7 × nParticles* **then**
15   f(x) ← penalty f(x);
16   **else**
17   **for** *parameters in objParams* **do**
18   f(x) ← f(x) + (weight(parameter—target)^2)
19   **end**
20   f(x) ← log(f(x)+ weight × nLoss) × M;
21   **return** f(x)

Algorithm 2: Optimization of magnet positions and strengths to minimize the objective function, `Objective`, defined in Algorithm 1.

```
/* Define the dipole positions (dipolePos) and
   strengths (dipoleStr), the start (startPos)
   and end (endPos) positions of the transfer
   line, the quantity of the quadrupoles,
   sextupoles and octupoles to include in the
   line (quadNumber, sextNumber, octNumber),
   and initial values for their positions and
   strengths (x_initial).                      /*
```
input: dipolePos, dipoleStr, startPos, endPos, quadNumber, sextNumber, octNumber, nParticles ← 5000, nIterations ← 10 000, $x_{initial}$
```
/* Optimize quadrupole positions and strengths
   /*
```
1 magnetList ← quadNumber of quadrupoles;
   init: quadPos, quadStr ← $x_{initial}$
2 objParams ← beam size, dispersion;
   optimize: `Objective` using GAs over nIterations → solution1
   init: quadPos, quadStr ← solution1
```
   /* Optimize quadrupole and sextupole
      positions/strengths                       /*
```
3 magnetList ← magnetList + sextNumber of sextupoles;
   optimize: `Objective` using Powell's method over nIterations → solution2
   init: quadPos, quadStr, sextPos, sextStr ← solution2
4 objParams ← objParams, beam size, dispersion;
   optimize: `Objective` using Powell's method over nIterations → solution2.1
   init: quadPos, quadStr, sextPos, sextStr ← solution2.1
```
   /* Optimize quadrupole, sextupole and
      octupole positions/strengths             /*
```
5 octNumber ← 0;
```
   /* If the objective function value has not
      yet reached the desired target value,
      test adding another octupole            /*
```
6 **while** $f(x) > target\ value$ **do**
7   magnetList ← magnet List + one octupole;
      optimize: `Objective` using Powell's method over nIterations → solution3
8   **if** *limited improvement* **then break**;
9 **end**
   init: quadPos, quadStr, sextPos, sextStr, octPos, octStr ← solution3
```
   /* Fine-tune solutions                       /*
```
10 nParticles ← 50 000;
   optimize: `Objective` using Powell's method over nIterations → solution3.1
   init: quadPos, quadStr, sextPos, sextStr, octPos, octStr ← solution3.1

---

[1] F. B. Taheri, M. Apollonio, R. Bartolini, J. Li, and B. Singh, Genetic optimisation of beamline design for DIAMOND, in *Proceedings of the 10th International Particle Accelerator Conference, IPAC-2019, Melbourne, Australia, 2019* (JACoW, Geneva, Switzerland, 2019), Vol. 19.

[2] M. Rossetti Conti, A. Bacci, A. Giribono, V. Petrillo, A. Rossi, L. Serafini, and C. Vaccarezza, Electron beam transfer line design for plasma driven free electron lasers, Nucl. Instrum. Methods Phys. Res., Sect. A **909**, 84 (2018).

[3] I. V. Bazarov and C. K. Sinclair, Multivariate optimization of a high brightness dc gun photoinjector, Phys. Rev. ST Accel. Beams **8**, 034202 (2005).

[4] L. Yang, D. Robin, F. Sannibale, C. Steier, and W. Wan, Global optimization of an accelerator lattice using multiobjective genetic algorithms, Nucl. Instrum. Methods Phys. Res., Sect. A **609**, 50 (2009).

[5] N. Neveu, L. Spentzouris, A. Adelmann, Y. Ineichen, A. Kolano, C. Metzger-Kraus, C. Bekas, A. Curioni, and P. Arbenz, Parallel general purpose multiobjective optimization framework with application to electron beam dynamics, Phys. Rev. Accel. Beams **22**, 054602 (2019).

[6] S. Reimann, M. Droba, O. Meusel, and H. Podlech, An algorithm for automated lattice design of transfer lines, J. Phys. Conf. Ser. **1350**, 012110 (2019).

[7] MAD-X, http://mad.web.cern.ch/mad/ (2021).

[8] J. A. Nelder and R. Mead, A simplex method for function minimization, Comput. J. **7**, 308 (1965).

[9] M. J. Powell, A new algorithm for unconstrained optimization, in *Nonlinear Programming* (Academic Press, New York, 1970), pp. 31–65.

[10] M. J. Powell, The BOBYQA algorithm for bound constrained optimization without derivatives, University of Cambridge, Cambridge NA Report No. DAMTP 2009/NA06, 2009.

[11] S. Appel and S. Reimann, Beam line optimization using derivative-free algorithms, J. Phys. Conf. Ser. **1350**, 012104 (2019).

[12] N. Neveu, J. Larson, J. Power, and L. Spentzouris, Photoinjector optimization using a derivative-free, model-based trust-region algorithm for the Argonne Wakefield Accelerator, J. Phys. Conf. Ser. **874**, 012062 (2017).

[13] A. Scheinker, S. Hirlaender, F. M. Velotti, S. Gessner, G. Z. Della Porta, V. Kain, B. Goddard, and R. Ramjiawan, Online multi-objective particle accelerator optimization of the AWAKE electron beam line for simultaneous emittance and orbit control, AIP Adv. **10**, 055320 (2020).

[14] R. Shalloo, S. Dann, J.-N. Gruse, C. Underwood, A. Antoine, C. Arran, M. Backhouse, C. Baird, M. Balcazar, N. Bourgeois *et al.*, Automation and control of laser wakefield accelerators using Bayesian optimization, Nat. Commun. **11**, 6355 (2020).

[15] X. Huang, J. Corbett, J. Safranek, and J. Wu, An algorithm for online optimization of accelerators, Nucl. Instrum. Methods Phys. Res., Sect. A **726**, 77 (2013).

[16] C. A. Lindstrøm, R. D'Arcy, M. J. Garland, P. Gonzalez, B. Schmidt, S. Schröder, S. Wesch, and J. Osterhoff, Matching small β functions using centroid jitter and two beam position monitors, Phys. Rev. Accel. Beams **23**, 052802 (2020).

[17] C. Emma, A. Edelen, M. J. Hogan, B. O'Shea, G. White, and V. Yakimenko, Machine learning-based longitudinal phase space prediction of particle accelerators, Phys. Rev. Accel. Beams **21**, 112802 (2018).

[18] A. Sanchez-Gonzalez, P. Micaelli, C. Olivier, T. Barillot, M. Ilchen, A. Lutman, A. Marinelli, T. Maxwell, A. Achner, M. Agåker *et al.*, Accurate prediction of x-ray pulse properties from a free-electron laser using machine learning, Nat. Commun. **8**, 15461 (2017).

[19] A. Hanuka, C. Emma, T. Maxwell, A. S. Fisher, B. Jacobson, M. J. Hogan, and Z. Huang, Accurate and confident prediction of electron beam longitudinal properties using spectral virtual diagnostics, Sci. Rep. **11**, 2945 (2021).

[20] E. Adli *et al.* (AWAKE Collaboration), Acceleration of electrons in the plasma wakefield of a proton bunch, Nature (London) **561**, 363 (2018).

[21] E. Gschwendtner *et al.* (AWAKE Collaboration), AWAKE, the advanced proton driven plasma wakefield acceleration experiment at CERN, Nucl. Instrum. Methods Phys. Res., Sect. A **829**, 76 (2016).

[22] E. Öz and P. Muggli, A novel Rb vapor plasma source for plasma wakefield accelerators, Nucl. Instrum. Methods Phys. Res., Sect. A **740**, 197 (2014).

[23] E. Adli *et al.* (AWAKE Collaboration), Experimental Observation of Proton Bunch Modulation in a Plasma at Varying Plasma Densities, Phys. Rev. Lett. **122**, 054802 (2019).

[24] M. Turner *et al.* (AWAKE Collaboration), Experimental Observation of Plasma Wakefield Growth Driven by the Seeded Self-Modulation of a Proton Bunch, Phys. Rev. Lett. **122**, 054801 (2019).

[25] F. Batsch *et al.* (AWAKE Collaboration), Transition between Instability and Seeded Self-Modulation of a Relativistic Particle Bunch in Plasma, Phys. Rev. Lett. **126**, 164802 (2021).

[26] K. Lotov, V. Minakov, and A. Sosedkin, Parameter sensitivity of plasma wakefields driven by self-modulating proton beams, Phys. Plasmas **21**, 083107 (2014).

[27] J. Schmidt, O. R. Jones, P. Muggli, M. Fraser, L. Jensen, B. Biskup, E. Gschwendtner, E. Bravin, A. Vorozhtsov, C. Bracco *et al.*, The AWAKE electron primary beam line, in *Proceedings of the 6th International Particle Accelerator Conference, IPAC-2015, Richmond, VA, 2015* (JACoW, Geneva, Switzerland, 2015).

[28] S.-Y. Kim, S. Doebert, O. Apsimon, R. Apsimon, G. Burt, M. Dayyani, S. Gessner, I. Gorgisyan, E. Granados, S. Mazzoni *et al.*, Commissioning of the electron injector for the AWAKE experiment, Nucl. Instrum. Methods Phys. Res., Sect. A **953**, 163194 (2020).

[29] P. Muggli for the AWAKE Collaboration, Physics to plan AWAKE Run 2, J. Phys. Conf. Ser. **1596**, 012008 (2020).

[30] E. Gschwendtner for the AWAKE Collaboration, AWAKE Run 2 at CERN, in *Proceedings of the 12th International Particle Accelerator Conference, IPAC-2021, Campinas, Brazil, 2021* (JACoW, Geneva, Switzerland, 2021).

[31] L. Verra *et al.* (AWAKE Collaboration), Controlled Growth of the Self-Modulation of a Relativistic Proton Bunch in Plasma, Phys. Rev. Lett. **129**, 024802 (2022).

[32] A. Caldwell and K. V. Lotov, Plasma wakefield acceleration with a modulated proton bunch, Phys. Plasmas **18**, 103101 (2011).

[33] A. A. Gorn, P. V. Tuev, A. V. Petrenko, A. P. Sosedkin, and K. V. Lotov, Response of narrow cylindrical plasmas to dense charged particle beams, Phys. Plasmas **25**, 063108 (2018).

[34] E. Adli (AWAKE Collaboration), Towards AWAKE applications: Electron beam acceleration in a proton driven plasma wake, in *Proceedings of the 7th International Particle Accelerator Conference, IPAC-2016, Busan, Korea, 2021* (JACoW, Geneva, Switzerland, 2021).

[35] V. K. Berglyd Olsen, E. Adli, and P. Muggli, Emittance preservation of an electron beam in a loaded quasilinear plasma wakefield, Phys. Rev. Accel. Beams **21**, 011301 (2018).

[36] K. Pepitone, S. Doebert, R. Apsimon, J. Bauche, M. Bernardini, C. Bracco, G. Burt, A. Chauchet, E. Chevallay, N. Chritin *et al.*, The electron accelerators for the AWAKE experiment at CERN-baseline and future developments, Nucl. Instrum. Methods Phys. Res., Sect. A **909**, 102 (2018).

[37] J. Farmer, L. Liang, R. Ramjiawan, F. M. Velotti, M. Weidl, E. Gschwendtner, and P. Muggli, Injection tolerances for AWAKE Run 2c, Technical Report, arXiv:2203.11622.

[38] E. Forest, F. Schmidt, and E. McIntosh, Introduction to the polymorphic tracking code, Report No. KEK-REPORT-2002-3, 2002.

[39] S. Kullback and R. A. Leibler, On information and sufficiency, Ann. Math. Stat. **22**, 79 (1951).

[40] M. Mitchell, *An Introduction to Genetic Algorithms* (MIT press, Cambridge, MA, 1998).

[41] K. Deb, A. Pratap, S. Agarwal, and T. Meyarivan, A fast and elitist multiobjective genetic algorithm: NSGA-II, IEEE Trans. Evol. Comput. **6**, 182 (2002).

[42] Py-BOBYQA: Derivative-free solver for bound-constrained minimization, https://github.com/numericalalgorithmsgroup/pybobyqa (2021).

[43] A. Karpatne, W. Watkins, J. Read, and V. Kumar, Physics-guided neural networks (PGNN): An application in lake temperature modeling, arXiv:1710.11431.

[44] E. Senes *et al.*, Recent AWAKE diagnostics development and operational results, in *Proceedings of the International Particle Accelerator Conference, IPAC '22, Bangkok, Thailand, 2022* (JACoW, Geneva, Switzerland, 2022).

[45] F. P. Asmus, F. M. Velotti, M. Turner, S. Gessner, M. Martyanov, C. Bracco, B. Goddard, and P. Muggli, Predicting the trajectory of a relativistic electron beam for external injection in plasma wakefields, in J. Phys. Conf. Ser. **1596**, 012048 (2020).

[46] C. Bracco, M. Aiba, B. Goddard, I. Gorgisyan, M. Turner, F. Velotti, and L. Verra, Systematic optics studies for the commissioning of the AWAKE electron beamline, in *Proceedings of the 10th International Particle Accelerator Conference, IPAC '19, Melbourne, Australia, 2019* (JACoW, Geneva, Switzerland, 2019).

[47] L. Verra, E. Gschwendtner, and P. Muggli, Study of external electron beam injection into proton driven plasma wakefields for AWAKE Run2, J. Phys. Conf. Ser. **1596**, 012007 (2020).

[48] D. E. Groom and S. Klein, Passage of particles through matter, Eur. Phys. J. C **15**, 163 (2000).

[49] M. B. Reid, Electron beam emittance growth in thin foils: A betatron function analysis, J. Appl. Phys. **70**, 7185 (1991).